Submitted to the
32nd International Conference on High Energy Physics
August 16 - 22, 2004, Beijing, China

Abstract: 6-0246 **Session: QCD soft interactions**

Deep inelastic diffractive scattering measured with the ZEUS Forward Plug Calorimeter

ZEUS Collaboration

10th August 2004

Abstract

Inclusive diffraction in deep inelastic scattering has been studied with the ZEUS detector at HERA using 1998-1999 data with an integrated luminosity of 4.2 pb^{-1}. The accessible range in hadronic mass, M_X, produced by diffractive dissociation of the exchanged photon, has been substantially increased by the installation of a forward plug calorimeter in the direction of the incoming proton. Results are presented for the kinematic range $2.2 < Q^2 < 80$ GeV^2, $37 < W < 245$ GeV and $M_X < 35$ GeV. The diffractive cross section, $\sigma^{\rm diff}_{\gamma^* p \to XN}(M_X, W, Q^2)/dM_X$, for $M_X < 2$ GeV shows a weak dependence on W and a strong decrease with Q^2 consistent with a higher twist behaviour. For larger M_X values, a strong rise with W and a leading twist behaviour are found. The comparison with the total $\gamma^* p$ cross section shows that at $W = 220$ GeV, diffraction with $M_X < 35$ GeV accounts for $19.8^{+1.5}_{-1.4}\%$ of $\sigma^{\rm tot}_{\gamma^* p \to XN}$ at $Q^2 = 2.7$ GeV^2, decreasing slowly to $10.1^{+0.6}_{-0.5}\%$ at $Q^2 = 27$ GeV^2. Fits of the form $d\sigma^{\rm diff}_{\gamma^* p \to XN}/dM_X \propto W^{a^{\rm diff}}$ show $a^{\rm diff}$ rising with Q^2 for $Q^2 > 10$ GeV^2. The analysis in terms of Pomeron exchange shows an intercept of the Regge trajectory, $\alpha_{I\!P}(0)$, lying halfway between $\alpha_{I\!P}(0) = 1$ and the $\alpha_{I\!P}(0)$ values deduced for the total $\gamma^* p$ cross section. The diffractive structure function of the proton is presented in terms of $x_{I\!P} F_2^{D(3)}(x_{I\!P}, \beta, Q^2)$. For $M_X < 2$ GeV, a weak dependence on $x_{I\!P}$ and a rapid decrease with Q^2 are found. At larger M_X, $x_{I\!P} F_2^{D(3)}$ shows a rapid rise as $x_{I\!P} \to 0$. For $M_X > 8$ GeV, $x_{I\!P} F_2^{D(3)}$ is constant with Q^2 and consistent with leading twist. The structure function of the Pomeron, defined as $F_2^{D(2)}(\beta, Q^2) = x_0 F_2^{D(3)}(x_0, \beta, Q^2)$ where $x_0 = 0.01$, has a maximum near $\beta = 0.5$ consistent with a $\beta(1-\beta)$ behaviour, suggesting that the main contribution comes from a Pomeron in a $q\bar{q}$ state. At $\beta < 0.1$, $F_2^{D(2)}$ rises as $\beta \to 0$ and as Q^2 increases, showing a pQCD-like evolution of the Pomeron structure function.

1 Introduction

Quantum Chromodynamics (QCD) in the perturbative DGLAP [1] expansion permits a precise description of structure functions measured in inclusive deep inelastic lepton-nucleon scattering (DIS). However, for the diffractive component of DIS, $ep \to e'XN$, (N = proton or low-mass excited nucleonic system) QCD is still far from achieving such success. The observation of events with a large rapidity gap at HERA provided the unprecedented opportunity to study diffractive scattering in DIS over a large range in spatial resolution and energy transfer between the lepton and the incoming proton. The spatial resolution is determined by the square of the four-momentum transfer ($-Q^2 = q^2$) from the electron to the hadronic system, XN. The energy dependence of the diffractive cross section is studied with respect to the c.m. energy, W, of the hadronic system. Contributions from specific vector mesons ($\rho^0, \omega, \phi, J/\Psi, ..$) and the onset of contributions from the excitation of the heavy quarks c, b are best studied using the mass M_X of the system X.

In a t-channel picture, diffraction is mediated by the exchange of a colourless object carrying the quantum numbers of the vacuum (at lowest order QCD a quark-antiquark or two-gluon system) between the virtual photon and the proton, known generically as the Pomeron. The analogue to the proton stucture function $F_2(x, Q^2)$, the diffractive structure function $F_2^{D(3)}$ [2], is parametrized in terms of Q^2, the momentum fraction $x_{I\!P}$ of the proton carried by the Pomeron, and the momentum fraction of the struck quark within the Pomeron, β, where $x_{I\!P} = [(P - N) \cdot q]/(P \cdot q) \approx (M_X^2 + Q^2)/(W^2 + Q^2)$ and $\beta = Q^2/[2(P - N) \cdot q] \approx Q^2/(M_X^2 + Q^2)$. The variables $x_{I\!P}$ and β are related to the Bjorken scaling variable x, the fraction of the proton momentum carried by the struck quark, by $x = \beta \cdot x_{I\!P}$. The data from this analysis are presented in terms of both sets of variables, (M_X, W, Q^2) and $(\beta, x_{I\!P}, Q^2)$.

In this analysis, inclusive diffraction in deep inelastic scattering (DIS) is studied using the M_X-method [3], [4]. High statistics measurements of DIS diffractive scattering over a wide kinematic range became accessible by the addition of a forward plug calorimeter (FPC) inside the ZEUS forward uranium calorimeter (FCAL). The FPC increased the accessible M_X range by a factor of about 1.7 and allowed a substantial reduction of contributions from high mass nucleon dissociation. The large range in M_X and Q^2 allows a detailed following of the evolution of the diffractive cross section. Results are presented for the kinematic range $37 < W < 245$ GeV, $M_X < 35$ GeV and $2.2 < Q^2 < 80$ GeV^2. The proton structure function F_2 as well as the total $\gamma^* p$ cross section have been measured allowing a direct comparison of the W and Q^2 dependences of diffractive and inclusive scattering.

2 Experimental set-up

The data were taken with the ZEUS detector at HERA in 1998/9 when electrons of 27.5 GeV collided with protons of 920 GeV. The analysis is based on an integrated luminosity of 4.2 pb^{-1}.
The ZEUS detector is described in detail elsewhere [5]. Events produced by deep inelastic scattering were identified using information from the uranium-scintillator calorimeter (CAL) consisting of the forward (FCAL), barrel (BCAL) and rear (RCAL) sections, the forward plug calorimeter (FPC), the central tracking detector (CTD), the small angle rear tracking detector (SRTD) [6] and the hadron-electron separator (RHES) which consists of a layer of 10000, 2.89×3.05 cm^2 silicon-pad detectors inserted in RCAL at a depth of 3.3 radiation lengths. The beam hole in the RCAL had been reduced to 20×8 cm^2 [7], which allowed detection of electrons scattered under small angles and hence small Q^2.

2.1 The Forward Plug Calorimeter

The FPC [8] was used to measure the energy of particles in the pseudorapidity range between $\eta = 4.0 - 5.0$. The FPC is a lead-scintillator sandwich calorimeter read out by wave length shifter (WLS) fibers and photomultipliers (PMT). It was installed in the 20×20 cm^2 beam hole of the forward uranium-scintillator calorimeter (FCAL) of the ZEUS detector. The FPC has outer dimensions of $192 \times 192 \times 1080$ mm^3 and a hole of 3.15 cm radius for the passage of the beams. The minimum angle for particle detection was 12 mrad which corresponds to a pseudorapidity of 5.1. In the FPC, lead plates of 15 mm thickness alternated with scintillator layers of 2.6 mm. The WLS fibers had 1.2 mm diameter and passed through 1.4 mm holes in the lead and scintillator layers. The holes were located on a 12 mm grid. The FPC was subdivided longitudinally into an electromagnetic (10 layers) and a hadronic section (50 layers) giving a total of 5.4 nuclear absorption lengths. The scintillator layers consisted of tiles forming towers which were read out individually. The cell cross sections were 24×24 mm^2 in the electromagnetic and 48×48 mm^2 in the hadronic section. The FPC was tested and calibrated with electron, muon and hadron beams. The energy resolution for electrons was $\sigma_E/E = (0.41 \pm 0.02)/\sqrt{E} \oplus 0.062 \pm 0.002$, ($E$ in GeV). When installed in the FCAL the energy resolution for pions was $\sigma_E/E = (0.65 \pm 0.02)/\sqrt{E} \oplus 0.06 \pm 0.01$ (E in GeV) and the e/h ratio was unity. The relative calibration of the FPC cells was regularly adjusted using measurements from a ^{60}Co source, which resulted in an average scale uncertainty of 4% (3%) for the EMC (HAC) cells [9].

3 Data selection and reconstruction of event kinematics

The reaction $e^-(k)\ p(P) \rightarrow e^-(k') +$ anything at fixed squared centre-of-mass energy, $s = (k+P)^2$, is described in terms of $Q^2 \equiv -q^2 = (k-k')^2$ and Bjorken $x = Q^2/(2(P \cdot q))$. At HERA $s \approx 4E_eE_p$, where $E_e = 27.5$ GeV and $E_p = 920$ GeV denote the electron and proton energies, leading to $\sqrt{s} = 318$ GeV. The fractional energy transferred to the proton in its rest system is $y = Q^2/(sx)$.

Scattered electrons were identified with an algorithm based on a neural network [10]. The direction and energy of the scattered electron were determined from the combined information given by CAL, SRTD, HES and CTD. The impact point of the electron on the face of the RCAL had to lie outside an area of 26.6×17 cm^2 (box cut) centered on the beam axis. Further cuts on the impact point were imposed to ensure reliable measurement of the electron energy. The minimum energy of the scattered electron was $E'_e > 10$ GeV.

The hadronic system was reconstructed from energy-flow objects (EFO) [11] which combine the information from tracks (CTD) and clusters (CAL). A minimum of 400 MeV of hadronic energy was required.

Corrections were applied for shower energy leaking across the RCAL beam hole from the scattered electron or the produced hadronic system.

The events studied in this analysis are of the type $ep \rightarrow e'X$ rest, where X denotes the hadronic system observed in the detector for rapidities $-3.5 < \eta < 5.2$, and rest the particle system escaping detection through the beam holes.

The value of Q^2 is reconstructed from the measured energy E'_e and scattering angle θ_e, of the electron,

$$Q^2 = 2E_eE'_e(1 + \cos\theta_e). \tag{1}$$

The value of W is reconstructed using the weighted average of the values determined from the electron and the hadron measurements. The mass M_X was determined by summing over all EFO's not assigned to the scattered electron,

$$M_X^2 = (\sum P_h)^2 \tag{2}$$

where P_h is the four-momentum vector of the EFO h.

The Z-coordinate of the event vertex was required to satisfy $-54 < Z_{\rm vtx} < 50$ cm. In order to reduce background from photoproduction, the requirement $46 < \sum_{i=e,h}(E_i - P_{Zi}) < 64$ GeV was imposed, where the sum is performed over the scattered electron and all hadronic

EFO's. A "minimum energy cut" was imposed on the hadronic system, requiring at least 0.4 GeV deposited in the RCAL outside of the first inner ring or in the BCAL; or $y_{JB}^{FB} = \sum_h (E_h - P_{Zh})/(2E_e)$ summing over all hadronic EFO's in FCAL plus BCAL to be $y_{JB}^{FB} > 0.004$.

Candidates for QED-Compton scattering consisting of a scattered electron and a photon with momentum balance in the plane transverse to the beams were removed.

The contamination from electron (proton) beam-gas scattering was negligible as measured using unpaired electron (proton) bunches.

A total of about 800,000 events passed the selection cuts. For the analysis, about 612,000 events with $2.2 < Q^2 < 80$ GeV^2, $37 < W < 245$ GeV and $M_X < 35$ GeV were used.

4 Data corrections

The data were corrected for detector acceptance and resolution by a suitable combination of several Monte Carlo (MC) models. Events from standard non-diffractive processes (nondif) were produced within the framework provided by DJANGOH 1.1 [12]. DJANGOH is interfaced to the MC programs HERACLES [13], LEPTO [14], ARIADNE [15] and JETSET [16] and includes QED and QCD radiative effects. The events have been generated using the CTEQ4D next-to-leading order parton density parametrizations [17] and setting the longitudinal structure function F_L of the proton to zero. Since the CTEQ4D parametrization does not reproduce the measured values for the proton structure function $F_2(x, Q^2)$ at $Q^2 < 2$ GeV^2 a parametrization of the measured F_2 data from Haidt [18] has been used to reweight the generated non-diffractive events.

Hadronic final states from diffractive DIS interactions, where the proton does not dissociate, $ep \to eXp$ (but excluding ρ^0 production via $ep \to e\rho^0 p$), were simulated with SATRAP which is based on the saturation model of Ref. [19] and interfaced to the RAPGAP framework [20]. The production of ρ^0 mesons, $ep \to e\rho^0 p$, was simulated with JETSET by adding the special module RHOP which uses the measured cross sections and production and decay angular distributions [21], [22].

The diffractive process in which the proton dissociates, $ep \to eXN$, was simulated with SATRAP by adding a special module called SANG [23]. The mass spectrum of the system N was generated according to $d\sigma/dM_X \propto (1/M_X^2)^\alpha$ with $\alpha \approx 1$. The fragmentation of the system N was simulated using JETSET. The reweighting procedure to match the MC predicted M_N spectrum for $M_N > 2.3$ GeV with that of the data is described below.

The non-diffractive and diffractive DIS processes were generated starting at $Q^2 = 0.5$ GeV^2.

To estimate the background from photoproduction, events were generated with PYTHIA [16] for $Q^2 < 0.1$ GeV^2 and $y > 0.6$. Events with lower values of y do not enter the data sample since the scattered electron, which escapes undetected through the rear beam hole, carries enough energy such that the hadronic system observed in the detector fails the cut on $\sum_i (E_i - P_{Zi})$.

First-order electroweak corrections for the non-diffractive and diffractive processes were generated with HERACLES.

The comparison of the number of events in the region $30 < \sum_i (E_i - P_{Zi}) < 46$ GeV observed in the data and predicted by MC for every (W, Q^2) bin provided an important check of the accuracy of the MC models, in particular at the lower values of Q^2.

The measurement of the total hadronic energy was validated by requiring a balance of the transverse momenta of the scattered electron and the observed total hadronic system. Transverse momentum balance, on average, was achieved by increasing the hadronic energies by a factor of 1.065, in agreement with the findings from MC simulation. The mass $M_X^{\rm meas}$, reconstructed from the energy-corrected EFO's, required an additional correction factor of 1.10 which was determined with MC simulated events.

The resolutions expected for the kinematical variables were estimated by MC simulation for diffractive events of the type $ep \to e'Xp$. For the Q^2, W and M_X bins considered in this analysis the r.m.s. resolutions are approximately given by $\frac{\sigma(Q^2)}{Q^2} = \frac{0.25}{(Q^2)^{1/3}}$, Q^2 in units of GeV^2 and $\frac{\sigma(W)}{W} = \frac{1.1}{W^{1/2}}$ GeV, $\sigma(M_X) = \frac{0.38}{M_X^{1/3}}$ GeV, with W, M_X in units of GeV.

The cross sections and structure functions are quoted at the following reference values:

- $Q^2_{\rm ref}$: 2.7, 4.0, 6.0, 8.0, 14.0, 27.0, 55.0 GeV^2;
- $W_{\rm ref}$: 45, 65, 85, 115, 150, 180, 220 GeV;
- $M_{X\rm ref}$: 1.2, 3.0, 6.0, 11.0, 20.0, 30 GeV.

4.1 Limiting the contribution from diffractive proton dissociation

In addition to single dissociation, $\gamma^* p \to Xp$, processes where the proton also dissociates, $\gamma^* p \to XN^{\rm dissoc}$, can contribute to the diffractive event sample. Events from double dissociation can be grouped into those where $N^{\rm dissoc}$ has a low mass, disappearing in the beam hole of the FPC without energy deposition in FPC or CAL, and those with a large mass where decay particles from $N^{\rm dissoc}$ deposit energy in the calorimeters. In the latter case, the reconstructed mass of the total hadronic system is larger than the mass of X. Such events lead to a distortion of the $\ln M_X^2$ distribution at high M_X values. In order to study this effect, double dissociative events were generated using SANG.

The parameters of SANG, in particular the shape of the M_N spectrum and the overall normalization were checked with a subset of the data that dominated the contribution from double dissociation. The study showed that, on average, events generated with a mass of the dissociated system $M_N < 2.3$ GeV deposit less than 1 GeV of energy in the FPC ($E_{\rm FPC}$), while events with $M_N > 2.3$ GeV deposit more than 1 GeV. Therefore, the contribution from double dissociation predicted by the reweighted SANG for $E_{\rm FPC} > 1$ GeV was subtracted from the data as a function of M_X, W and Q^2. It was less than 5% for $M_X/W < 0.05$, 15% at $M_X/W = 0.1$ and 31% at $M_X/W = 0.14$. The diffractive cross section presented below is therefore the sum of the contributions from the Xp and $XN, M_N < 2.3$ GeV contributions.

5 Extraction of the diffractive contribution

The diffractive contribution was extracted from the data using the M_X method [3], [4], which is based on the fact that the diffractive and non-diffractive contributions have very different $\ln M_X^2$ distributions as shown in Fig. 1. The diffractive contribution is the plateau-like structure at low $\ln M_X^2$ while the non-diffractive contribution peaks at high $\ln M_X^2$ and has an exponential fall-off towards the lower M_X values, $dN/d\ln M_X^2 \propto \exp(b \ln M_X^2)$. The peak position scales in $\ln(M_X^2/W^2)$ and the slope b is approximately independent of W and Q^2. These characteristics are properties of events with uniform, random and uncorrelated particle production along the rapidity axis. The exponential in $\ln M_X^2$ and the scaling in $\ln(M_X^2/W^2)$ are directly connected to the exponential suppression of large rapidity gaps by QCD radiation.

The diffractive contribution was defined to be the excess of events at lower M_X above the exponential fall-off of the non-diffractive contribution in $\ln M_X^2$. The exponential fall permits the subtraction of the non-diffractive contribution and, therefore, the extraction of the diffractive contribution without assuming the precise M_X dependence of the latter. The distribution is of the form:

$$\frac{dN}{d\ln M_X^2} = D + c \cdot \exp(b\ \ln M_X^2),\ \ln M_X^2 < \ln W^2 - \eta_0, \tag{3}$$

where D is the diffractive contribution and the second term the non-diffractive contribution. The quantity $(\ln W^2 - \eta_0)$ specifies the maximum value of $\ln M_X^2$ up to which the exponential behaviour of the non-diffractive contribution holds. A value of $\eta_0 = 1.8$ was found from the data. Equation 3 is applied to the data in the limited range $\ln W^2 - 5.5 < \ln M_X^2 < \ln W^2 - \eta_0$ to determine the parameters b and c. The diffractive contribution was not taken from the fit but was obtaineded by subtracting from the observed number of events the non-diffractive contribution determined from the fitted values of b and c.

The diffractive contribution is expected to be a slowly varying function of $\ln M_X^2$ when $M_X^2 > Q^2$ and to approach, in the asymptotic limit, a constant $\ln M_X^2$ distribution at large M_X. Therefore, D was assumed to be constant over the limited M_X range $\ln W^2 - 5.5 < \ln M_X^2 < \ln W^2 - \eta_0$. The non-diffractive contribution in the (M_X, W, Q^2) bins was measured in two steps. In the first step, the slope b was determined as an average over the fits to the data for the intervals with W between 134 and 245 GeV and Q^2 between 2.2 and 10 GeV^2. The fits yielded $b_{\text{nom}} = 1.67 \pm 0.07$. In the second step, the fits were repeated for all (W, Q^2) intervals, using $b = b_{\text{nom}}$ as fixed parameter and assuming D to be constant.

6 Evaluation of the cross sections

For the final analysis, only bins where the fraction of non-diffractive background was less than 50% were kept. The average differential cross section for ep scattering in a given (M_X, W, Q^2) bin was obtained by correcting the number of diffractive events for acceptance and smearing.

The systematic uncertainties of the cross sections were estimated by varying the cuts and the algorithms used to select the events - at the levels of data and MC simulation - and repeating the full analysis for 16 systematic variants. The total systematic error for each bin was determined by adding quadratically the individual systematic uncertainties, separately for the positive and negative contributions. The total errors were then given by adding the statistical and systematic errors in quadrature.

7 The proton structure function F_2 and the total $\gamma^* p$ cross section

The differential cross section for inclusive ep scattering mediated by virtual photon exchange is given in terms of the structure functions F_i of the proton:

$$\frac{d^2\sigma^{e^-p}}{dxdQ^2} = \frac{2\pi\alpha^2}{xQ^4}[Y_+F_2(x,Q^2) + Y_-xF_3(x,Q^2) - y^2F_L(x,Q^2)](1+\delta_r(x,Q^2)) \tag{4}$$

where $Y_\pm = 1 \pm (1-y)^2$ and x and Q^2 are defined at the hadronic vertex. In the Q^2 range considered in this analysis, $Q^2 < 80$ GeV^2, the contributions from Z^0 exchange and Z^0 -

γ interference are well below 1%. In the above equation, F_L is the longitudinal structure function. The contribution of F_L to the cross section relative to that from F_2 is given by $\frac{y^2}{1+(1-y)^2}\frac{F_L}{F_2}$. The F_L measurements and the results on F_L from a QCD fit to the structure function data by H1 [24], together with similar results from a QCD fit by ZEUS [25], have been approximated by $F_L = 0.2F_2$. The longitudinal contribution in the highest y (= lowest x) bin of this analysis is found to be 3.8%, decreasing to 1.5% for the next to highest y-bin. For the other bins, the F_L contribution is below 1%.

The F_2 values measured in this analysis are shown in Fig. 2 together with those from previous measurements. Good agreement is observed over the full x range at all Q^2-values. The proton structure function F_2 rises rapidly as $x \to 0$ for all values of Q^2.

For comparison with the diffractive cross section, the total cross section for virtual photon proton scattering,

$$\sigma^{\mathrm{tot}}_{\gamma^* p} \equiv \sigma_T(x, Q^2) + \sigma_L(x, Q^2) \tag{5}$$

has been extracted from the F_2 measurements using

$$\sigma^{\mathrm{tot}}_{\gamma^* p} = \frac{4\pi^2\alpha}{Q^2(1-x)} F_2(x, Q^2) \tag{6}$$

which is valid for $4m_p^2 x^2 \ll Q^2$ [26].

8 Differential cross section for $\gamma^* p \to XN$

The cross section for the process $ep \to eXN$ can be expressed in terms of the transverse (T) and longitudinal (L) cross sections, σ_T^{diff} and σ_L^{diff}, for $\gamma^* p \to XN$ as

$$\frac{d\sigma^{\mathrm{diff}}_{\gamma^* p \to XN}(M_X, W, Q^2)}{dM_X} \equiv \frac{d(\sigma_T^{\mathrm{diff}} + \sigma_L^{\mathrm{diff}})}{dM_X} \approx \frac{2\pi}{\alpha}\frac{Q^2}{(1-y)^2+1}\frac{d\sigma^{\mathrm{diff}}_{ep \to eXN}(M_X, W, Q^2)}{dM_X d\ln W^2 dQ^2}. \tag{7}$$

Here, a term $[1 - \frac{y^2}{(1-y)^2+1}\frac{\sigma_L^{\mathrm{diff}}}{\sigma_T^{\mathrm{diff}}+\sigma_L^{\mathrm{diff}}}]$ multiplying $[\sigma_T^{\mathrm{diff}} + \sigma_L^{\mathrm{diff}}]$ has been neglected. Since $y \approx W^2/s$, the effect is less than 4% for $W < 200$ GeV, and 7% in the highest W bin, 200 - 245 GeV, if $\sigma_L^{\mathrm{diff}} < 0.5\ \sigma_T^{\mathrm{diff}}$.[1]

The diffractive cross section for $\gamma^* p \to XN$, where $M_N < 2.3$ GeV, is presented in Fig. 3. Compared to the previous ZEUS analysis of this type [4], a factor of four more data points and a large increase in the kinematic range is achieved.

[1] The processes $\gamma^* p \to Vp$, $V = \rho^0, \phi$ contribute about one third of the diffractive cross section measured in the lowest M_X bin ($M_X < 2$ GeV) and are dominated by longitudinal photon production. Under the assumption that these are the only contributions from longitudinal photons $\sigma_L^{\mathrm{diff}} < 0.5\ \sigma_T^{\mathrm{diff}}$ at $M_X < 2$ GeV. The measured data on J/Ψ-production indicate that this process contributes less than 10% of the diffractive cross section in the bin $M_X = 2 - 4$ GeV.

8.1 W dependence of the diffractive cross section

For $M_X < 2$ GeV, the diffractive cross section $d\sigma^{\rm diff}/dM_X$ is rather constant with W. By contrast, at higher M_X, up to $8 < M_X < 15$ GeV, a strong rise with W is observed for all values of Q^2. This was quantified by fitting the data for each Q^2, M_X bin with $M_X < 15$ GeV to the form

$$\frac{d\sigma^{\rm diff}_{\gamma^* p \to XN}}{dM_X} = h \cdot W^{a^{\rm diff}} \tag{8}$$

with h and $a^{\rm diff}$ treated as free parameters. The resulting $a^{\rm diff}$ values are shown in Fig. 4 for the different M_X intervals as a function of Q^2. For $M_X > 4$ GeV there is a clear tendency for $a^{\rm diff}$ to rise with Q^2.

In Regge models, soft diffraction is described by the exchange of the Pomeron trajectory, $\alpha_{I\!P}(t)$: $d\sigma/dt \propto e^{(2\alpha_{I\!P}(t)-2)\cdot \ln(s/s_0)+f(t)}$ where t is the four-momentum transfer squared from γ^* to X, $t = (\gamma^* - X)^2$, $f(t)$ characterizes the t-dependencies of the pN and $\gamma^* X$ vertices, and $s_0 = 1$ GeV^2. The t - averaged $\alpha_{I\!P}(t)$ is related to $a^{\rm diff}$ via $\overline{\alpha_{I\!P}} = 1 + a^{\rm diff}/4$, Hadron-hadron scattering leads to $\alpha^{\rm soft}_{I\!P}(0) = 1.096^{+0.012}_{-0.009}$ [27]. Averaging over t reduces this value by about 0.02 leading to $\overline{\alpha^{\rm soft}_{I\!P}} = 1.076^{+0.012}_{-0.009}$ and to $a^{\rm soft} = 0.302^{+0.048}_{-0.036}$. This is shown in Fig. 4 by the shaded band marked 'soft Pomeron'. For $0 < M_X < 2$ GeV, the data are in good agreement with this expectation. For $Q^2 > 10$ GeV^2 and $M_X > 2$ GeV, however, $a^{\rm diff}$ lies above $a^{\rm soft}$, the probability for $a^{\rm diff} \leq a^{\rm soft}$ being less than 0.1 %. The data give clear evidence for $a^{\rm diff}$ rising with Q^2.

In Figure 5 the Q^2-dependence of $\alpha^{\rm tot}_{I\!P}(0)$ obtained in this analysis from the W-dependence of the total $\gamma^* p$-cross section, $\alpha^{\rm tot}_{I\!P}(0) = 1 + \lambda$, is compared with $\alpha^{\rm diff}_{I\!P}(0) = \overline{\alpha_{I\!P}} + 0.02$ obtained from the diffractive cross section for $4 < M_X < 8$ GeV. Both measurements are above the soft Pomeron band. The diffractive result lies approximately half-way in between the soft Pomeron and the result obtained from $\sigma^{\rm tot}_{\gamma^* p}$ which is in contradistinction to the naive expectation of equal $\alpha_{I\!P}(0)$ values for the two processes. In other words, the Pomeron trajectory extracted for diffraction is half as steep as that obtained from $\sigma^{\rm tot}_{\gamma^* p}$. The diffractive data are well described by the shaded band which represents 'half' of the W rise of the total cross section: $\alpha_{I\!P}(0) = 1 + \lambda/2$. In other words, for $M_X > 2$ GeV, the diffractive cross section has approximately the same W dependence as the total cross section.

8.2 M_X dependence of the diffractive cross section

The M_X dependence of the diffractive cross section for $W = 220$ GeV is shown in Fig. 6 for different values of Q^2. The highest W region is used since it provides the largest range in M_X. The cross section has been multiplied by a factor of Q^2 since a leading twist behaviour would give an approximate constancy as a function of Q^2. The region of M_X below about 6 GeV shows a rapid decrease with Q^2 which is evidence for a predominantly higher twist behaviour. Above $M_X = 11$ GeV, little dependence on Q^2 is observed. In this region diffraction is of leading twist.

8.3 Diffractive contribution to the total cross section

The ratio of the diffractive cross section to $\gamma^* p$ cross section,

$$r_{\rm tot}^{\rm diff} \equiv \frac{\sigma^{\rm diff}}{\sigma^{\rm tot}} = \frac{\int_{M_a}^{M_b} dM_X d\sigma^{\rm diff}_{\gamma^* p \to XN, M_N < 2.3 {\rm GeV}} / dM_X}{\sigma^{\rm tot}_{\gamma^* p}} \tag{9}$$

was derived for all M_X bins, with $\sigma^{\rm tot}_{\gamma^* p}$ taken from this analysis. The ratio $r_{\rm tot}^{\rm diff}$ is shown in Fig. 7. Different W and Q^2 behaviour is observed for different M_X regions. For $M_X < 2$ GeV, $r_{\rm tot}^{\rm diff}$ is falling or constant with W, while for the higher M_X bins, it is constant or even slightly increasing with W. The low M_X bins exhibit a strong decrease of $r_{\rm tot}^{\rm diff}$ with increasing Q^2, while, for $M_X > 4$ GeV, this decrease becomes less dramatic and for $M_X > 8$ GeV almost no Q^2 dependence is observed. Here, the diffractive cross section has approximately the same W and Q^2-dependence as the total cross section, in agreement with the conclusion drawn from Fig. 5.

The ratio of the total observed diffractive cross section to the total cross section, $\sigma^{\rm diff}_{obs}(M_X < 35 \text{ GeV}, M_N < 2.3 \text{ GeV})/\sigma^{\rm tot}$, has been evaluated as a function of Q^2 for the highest W bin, $W = 200 - 245$ GeV, which provides the highest reach in the diffractive mass M_X: $0 < M_X < 35$ GeV. The diffractive contribution is a substantial fraction of the total cross section as can be seen from $\sigma^{\rm diff}_{obs}(M_X < 35 \text{ GeV}, M_N < 2.3 \text{ GeV})/\sigma^{\rm tot}$, which reaches

- $19.8^{+1.5}_{-1.4}\%$ at $Q^2 = 2.7$ GeV^2,
- $16.5^{+1.0}_{-0.9}\%$ at $Q^2 = 4$ GeV^2,
- $14.0^{+0.8}_{-0.8}\%$ at $Q^2 = 8$ GeV^2,
- $12.3^{+0.8}_{-0.8}\%$ at $Q^2 = 14$ GeV^2,
- $10.1^{+0.6}_{-0.7}\%$ at $Q^2 = 27$ GeV^2.

9 Diffractive structure function of the proton

The diffractive structure function of the proton can be related to the diffractive cross section for $W^2 \gg Q^2$ as follows:

$$\frac{1}{2M_X}\frac{d\sigma^{\rm diff}_{\gamma^* p\to XN}(M_X,W,Q^2)}{dM_X} = \frac{4\pi^2\alpha}{Q^2(Q^2+M_X^2)} x_{I\!P} F_2^{D(3)}(\beta, x_{I\!P}, Q^2) \tag{10}$$

If $F_2^{D(3)}$ is interpreted in terms of quark densities, it specifies the probability to find, in a diffractive process, a quark carrying a momentum fraction $x = \beta x_{I\!P}$ of the proton momentum.

Figure 8 shows $x_{I\!P} F_2^{D(3)}$ as a function of $x_{I\!P}$ for different selections of β and Q^2. For the lowest M_X region which corresponds to high β, little dependence on $x_{I\!P}$ is observed, in contrast to lower β selections where $x_{I\!P} F_2^{D(3)}$ rises strongly as $x_{I\!P} \to 0$ reflecting the rapid increase of the diffractive cross section with rising W. The strong increase of $x_{I\!P} F_2^{D(3)}$ as $x_{I\!P} \to 0$ is reminiscent of the rise of the proton structure function $F_2(x, Q^2)$ as $x \to 0$ which in pQCD is attributed to the rapid increase of the gluon density in the proton as $x \to 0$.

9.1 The structure function of the Pomeron $F_2^{D(2)}(\beta, Q^2)$

It has been suggested [2] that $F_2^{D(3)}(x_{I\!P}, \beta, Q^2)$ should factorize into a term which depends on the probability of finding a Pomeron carrying a fraction $x_{I\!P}$ of the proton momentum, and the structure function of the Pomeron, $F_2^{D(2)}$, given in terms of the quark densities of the Pomeron which depend on β and Q^2:

$$F_2^{D(3)}(x_{I\!P}, \beta, Q^2) = f_{I\!P}(x_{I\!P}, Q^2) \cdot F_2^{(D(2)}(\beta, Q^2) \tag{11}$$

where $f_{I\!P}(x_{I\!P}, Q^2)$ is generically called the Pomeron flux factor. In this model, the flux factor is assumed to be of the form

$$f_{I\!P}(x_{I\!P}, Q^2) = (C/x_{I\!P}) \cdot (x_0/x_{I\!P})^{n(Q^2)}, \tag{12}$$

and taking for the arbitrary normalization constant $C = 1$ leads to

$$F_2^{D(2)}(\beta, Q^2) = x_0 \cdot F_2^{D(3)}(x_0, \beta, Q^2). \tag{13}$$

We note that this form gives a good description of the data, see below.

The values of $F_2^{D(2)}(\beta, Q^2)$ were extracted from the data as follows. For a given (Q^2, β) combination, those $x_{I\!P} F_2^{D(3)}$ measurements with $0.5 \cdot x_0 < x_{I\!P} < 1.5 \cdot x_0$ were selected. For each measurement selected, the $x_{I\!P} F_2^{D(3)}$ value measured at $x_{I\!P\,meas}$ was transported to $x_{I\!P} = x_0$ using the BEKW(mod) fit (see Eq. 19 below). On average, the difference between measured and transported value was of the order of 5%. Finally, for every (Q^2, β) point the weighted average of the selected measurements was determined.

The resulting measurements of $F_2^{D(2)}(\beta, Q^2)$ are presented in Fig. 9. Several aspects are noteworthy. Firstly, there is a large contribution from the valence region, $\beta > 0.2$. In fact, $F_2^{D(2)}(\beta, Q^2)$ has a maximum near $\beta = 0.5$ consistent with a $\beta(1-\beta)$ variation. This suggests strongly that the lowest state of the Pomeron in this process is $q\overline{q}$. The data indicate also that the region of high β decreases as Q^2 increases from 14 - 27 GeV^2. For $\beta < 0.1$, $F_2^{D(2)}$ is seen to rise as $\beta \to 0$, and to rise with increasing Q^2. This behaviour is very similar to that of the proton structure function F_2.

9.2 Comparison with the BEKW model

The BEKW model [28] parametrises the diffractive cross section in terms of $q\overline{q}$ and $q\overline{q}g$) dipoles produced by transverse and longitudinal photons, interacting with the proton. Specifically,

$$x_{I\!P} F_2^{D(3)}(\beta, x_{I\!P}, Q^2) \quad = \quad c_T \cdot F_{q\overline{q}}^T + c_L \cdot F_{q\overline{q}}^L + c_g \cdot F_{q\overline{q}g}^T \tag{14}$$

where

$$F_{q\overline{q}}^T \quad = \quad (\frac{x_0}{x_{I\!P}})^{n_T(Q^2)} \cdot \beta(1-\beta) \tag{15}$$

$$F_{q\overline{q}}^L \quad = \quad (\frac{x_0}{x_{I\!P}})^{n_L(Q^2)} \cdot \frac{Q_0^2}{Q^2 + Q_0^2} \cdot [\ln(\frac{7}{4} + \frac{Q^2}{4\beta Q_0^2})]^2 \cdot \beta^3(1-2\beta)^2 \tag{16}$$

$$F_{q\overline{q}g}^T \quad = \quad (\frac{x_0}{x_{I\!P}})^{n_g(Q^2)} \cdot \ln(1 + \frac{Q^2}{Q_0^2}) \cdot (1-\beta)^{\gamma}. \tag{17}$$

The original BEKW model includes also a higher twist term for $(q\overline{q})$ produced by transverse photons. Since we found that our data are insensitive to this term, it has been neglected. The coefficients c_T, c_L, c_g are to be determined from experiment. For $F_{q\overline{q}}^L$ we have replaced the term $\frac{Q_0^2}{Q^2}$ provided by BEKW by the factor $\frac{Q_0^2}{Q^2+Q_0^2}$ to avoid problems as $Q^2 \to 0$. The strong rise of $\alpha_{I\!P}(0)$ with $\ln Q^2$ observed in the present data suggested to use for $n(Q^2)$ the form :

$$n(Q^2) \quad = \quad n_0 + n_1 \ln(1 + \frac{Q^2}{Q_0^2}). \tag{18}$$

This modified BEKW form will be refered to as BEKW(mod). Fits were performed by adding the statistical and systematic errors in quadrature. Taking $x_0 = 0.01$ and $Q_0^2 = 0.4$

GeV^2, the BEKW form gives an excellent description of the data, viz. $\chi^2 = 127$ for 193 $d.o.f$. The fit showed n_0 and n_1 for the longitudinal component to be zero, within errors. The fit showed also that, within errors, $n(Q^2)$ is the same for the T and g contributions, viz. $n_1^T = 0.0659 \pm 0.0037$ and $n_1^g = 0.0686 \pm 0.0125$, which implies that the Pomeron flux is the same for the $(q\overline{q})$ and $(q\overline{q}g)$ components produced by transverse photons. This led finally to the following results:

$$\begin{aligned} c_T &= 0.117 \pm 0.003 \\ c_L &= 0.171 \pm 0.012 \\ c_g &= 0.00926 \pm 0.00033 \\ n_1^{T,g} &= 0.0662 \pm 0.0032 \\ \gamma &= 8.32 \pm 0.51 \end{aligned} \tag{19}$$

with $\chi^2 = 132$ for 198 $d.o.f$. The value of the power $\gamma = 8.32 \pm 0.51$ is considerably larger than the value of about three expected by BEKW.

Figure 10 compares the measurements of $x_{I\!P} F_2^{D(3)}(\beta, x_{I\!P}, Q^2)$ with the BEKW(mod) fit. The large and medium β regions are dominated by the $(q\overline{q})$ contribution produced by transverse photons. For $\beta < 0.1$, the dominant contribution is due to $(q\overline{q}g)$ production by transverse photons.

Figure 11 compares the BEKW(mod) fit with the measurements of $F_2^{D(2)}$. In general, the BEKW(mod) curves describe the data well. However, as $\beta \to 0$ the data tend to rise more rapidly with rising Q^2 than predicted by the BEKW(mod) fit. The dominating term at small values of β is $F^T_{q\overline{q}g}$.

A better description of the low β region can be obtained by replacing the $q\overline{q}g$-term of the BEKW model, $F^T_{q\overline{q}g}$, by the following radiation term:

$$F_{\rm rad} = (\frac{x_0}{x_{I\!P}})^{n^{\rm xrad}(Q^2)}[(\frac{1}{\beta})^{n^{\beta \rm rad}(Q^2)} - 1](1-\beta)^\gamma \tag{20}$$

The constant β_0 was taken to be 0.1. The $x_{I\!P}$ dependence for $F_{\rm rad}$ was assumed to be the same as for $F_{q\overline{q}}$, $n^{\rm xrad}(Q^2) = n_1^T \cdot \ln(1 + \frac{Q^2}{Q_0^2})$. The power $n^{\beta \rm rad}$ was assumed to be of the form $n^{\beta \rm rad}(Q^2) = n_1^R \cdot \ln(1 + \frac{Q^2}{Q_0^2})$. Treating $c_T, c_L, c_{\rm rad}, n_1^T, n_1^R$ and γ as free parameters - where $c_{\rm rad}$ is the factor multiplying $F_{\rm rad}$ - the fit yielded:

$$
\begin{aligned}
c_T &= 0.1128 \pm 0.0012 \\
c_L &= 0.178 \pm 0.011 \\
c_{\mathrm{rad}} &= 0.116 \pm 0.024 \\
n_1^T &= 0.0682 \pm 0.0016 \\
n_1^R &= 0.0175 \pm 0.0034 \\
\gamma &= 2.90 \pm 0.22
\end{aligned}
\tag{21}
$$

with $\chi^2 = 144$ for 196 d.o.f. It is noteworthy that the replacement of the $q\bar{q}g$ term by the radiation term gives a good description of the data. Furthermore, γ, the power of the $(1-\beta)$ factor agrees with the value of three expected by BEKW. The fit results are compared in Fig. 12 with the $F_2^{D(2)}$ measurements. Good overall agreement with the data as well as agreement with the trend of the data as $\beta \to 0$ and/or as Q^2 increases is now obtained.

10 Summary

Results have been presented on the proton structure function and on diffraction in deep inelastic scattering. Diffraction has been measured over a substantially larger kinematic region compared to our previous M_X - analysis, namely $2.2 < Q^2 < 80$ GeV^2, $37 < W < 245$ GeV and $M_X < 35$ GeV, as a result of the addition of a forward plug calorimeter (FPC). The FPC has also allowed tighter control over diffractive double dissociation, limiting its contribution to $M_N < 2.3$ GeV.

From proton structure function $F_2(x, Q^2)$ the total cross section $\sigma^{\mathrm{tot}}_{\gamma^* p}$ has been deduced as a function of Q^2 and W, and has been analyzed in terms of the intercept of the Pomeron trajectory, $\alpha_{I\!P}(0)$. A strong rise of $\alpha_{I\!P}(0)$ with Q^2 is observed.

The diffractive cross section is presented in terms of Q^2, W and M_X. For $M_X < 2$ GeV, $\frac{d\sigma^{\mathrm{diff}}_{\gamma^* p \to XN}(M_X, W, Q^2)}{dM_X}$ shows only a weak dependence on W but a strong decrease with Q^2. For $M_X > 2$ GeV, a strong rise with W is observed while the dependence on Q^2 becomes weak as M_X increases. The analysis in terms of $Q^2 \frac{d\sigma^{\mathrm{diff}}_{\gamma^* p \to XN}}{dM_X}$ as a function of M_X shows for $M_X < 2$ GeV a rapid decrease with Q^2, characteristic for a higher twist behaviour. For $M_X > 8$ GeV, almost no dependence on Q^2 is observed which shows that in this region diffraction scattering is of leading twist.

The Q^2 and W behaviour of the diffractive and total cross sections has also been studied in terms of the ratio $r^{\mathrm{diff}}_{\mathrm{tot}} \equiv \frac{\sigma^{\mathrm{diff}}}{\sigma^{\mathrm{tot}}}$. For $M_X < 2$ GeV, $r^{\mathrm{diff}}_{\mathrm{tot}}$ is falling with W while for

$M_X > 2$ GeV it is independent of W. In terms of Q^2, $r_{\rm tot}^{\rm diff}$ is falling rapidly with Q^2 for $M_X < 2$ GeV, while for $M_X > 8$ GeV $r_{\rm tot}^{\rm diff}$ is approximately constant with Q^2. The comparison of the diffractive contribution *observed* for $M_X < 35$ GeV with the total cross section shows that for $W = 220$ GeV diffraction contributes at least $19.8^{+1.5}_{-1.4}\%$ to $\gamma^* p$ scattering at $Q^2 = 2.7$ GeV^2. With increasing Q^2 the diffractive contribution decreases slowly reaching $10.1^{+0.6}_{-0.7}\%$ at $Q^2 = 27$ GeV^2.

Fits of the diffractive cross section to the form $\frac{d\sigma^{\rm diff}_{\gamma^* p \to XN}}{dM_X} = h \cdot W^{a^{\rm diff}}$ show strong evidence for $a^{\rm diff}$ rising with Q^2, once Q^2 is above 10 GeV^2. The analysis in terms of Pomeron exchange shows the resulting intercept of the Regge trajectory, $\alpha_{I\!P}(0)$, lies halfway between $\alpha_{I\!P}(0) = 1$ and the $\alpha_{I\!P}(0)$ values deduced for the total $\gamma^* p$ cross section.

The diffractive structure function of the proton, multiplied by $x_{I\!P}$, $x_{I\!P} F_2^{D(3)}(x_{I\!P}, \beta, Q^2)$, has been measured as a function of $x_{I\!P}$ and Q^2 for different values of M_X. For $M_X < 2$ GeV, the diffractive structure function is approximately constant as a function of $x_{I\!P}$ and rapidly decreasing with Q^2. For $M_X > 2$ GeV, $x_{I\!P} F_2^{D(3)}$ increases rapidly as $x_{I\!P} \to 0$ but is rather constant as a function of Q^2 which indicates higher twist behaviour for $M_X < 2$ GeV, leading twist behaviour for $M_X > 8$ GeV and a transition region in between.

A good description of the data is obtained by a fit with a modified version of the BEKW model. It is remarkable that, within errors, the fit yields the same Pomeron flux for the $(q\overline{q})$ and $(q\overline{q}g)$ contributions produced by transverse photons where the Pomeron flux is assumed to be of the form $1/x_{I\!P} \cdot (x_{I\!P}/x_0)^{1+\ln Q^2/Q_0^2}$. Within the model, the diffractive structure function at low and medium values of β is dominated by diffractive contributions from transverse photons. At low $\beta < 0.1$, the largest contribution to $x_{I\!P} F_2^{D(3)}$ results from $(q\overline{q}g)$ production. As β increases, the $(q\overline{q})$ - contribution becomes more important. The contribution from production by longitudinal photons is only substantial at $\beta > 0.9$.

The structure function of the Pomeron, defined as $F_2^{D(2)}(\beta, Q^2) = x_0 F_2^{D(3)}(x_0, \beta, Q^2)$, with $x_0 = 0.01$, shows several remarkable properties. In the valence region, $\beta > 0.1$, it exhibits a maximum near $\beta = 0.5$ consistent with a $\beta(1-\beta)$ variation, suggesting that the main contribution comes from a Pomeron in a $q\overline{q}$ state. There is also an indication that $F_2^{D(2)}$ decreases at high β as Q^2 increases. In the sea region, $\beta < 0.1$, $F_2^{D(2)}$ is rising as $\beta \to 0$, and is rising as Q^2 increases. These features observed at high and low β strongly suggest a pQCD-like evolution of the Pomeron structure function $F_2^{D(2)}(\beta, Q^2)$ with β and Q^2. A QCD-inspired radiation term gives a good decription of $x_{I\!P} F_2^{D(3)}$ and $F_2^{D(2)}$.

References

[1] V.N. Gribov and L.N. Lipatov, Sov. J. Nucl. Phys. **15**, 675 (1972);
Yu.L. Dokshitzer, Sov. Phys. JETP **46**, 641 (1977);
G. Altarelli and G. Parisi, Nucl. Phys. **B 126**, 298 (1977).

[2] G. Ingelman and P.E. Schlein, Phys. Lett. **B 152**, 256 (1985).

[3] ZEUS Coll., M. Derrick et al., Z. Phys. **C 70**, 391 (1996).

[4] ZEUS Coll., J. Breitweg et al., Eur. Phys. J. **C 6**, 43 (1999).

[5] ZEUS Coll., M. Derrick et al., Phys. Lett. **B 293**, 465 (1992).

[6] A. Bamberger et al., Nucl. Inst. Meth. **A 401**, 63 (1997).

[7] ZEUS Coll., S. Chekanov et al., Eur. Phys. J. **C 21**, 443 (2001).

[8] ZEUS Coll., FPC group, A. Bamberger et al., Nucl. Inst. Meth. **A 450**, 235 (2000).

[9] F. Goebel, *Measurement of the Diffractive Contribution to the DIS Cross Section Using the ZEUS Forward Plug Calorimeter*. Ph.D. Thesis, Hamburg University, Hamburg (Germany), Report DESY-THESIS-2001-049, 2001.

[10] H. Abramowicz, A. Caldwell and R. Sinkus, Nucl. Inst. Meth. **A 365**, 508 (1995).

[11] G.M. Briskin, *Diffrac Dissociation in ep Deep Inelastic Scattering*. Ph.D. Thesis, University of Tel Aviv, Tel Aviv (Israel), Report DESY-THESIS-1998-036, 1998.

[12] K. Charchula, G.A. Schuler and H. Spiesberger, Comp. Phys. Comm. **81**, 381 (1994).

[13] A. Kwiatkowski, H. Spiesberger and H.-J. Möhring, Comp. Phys. Comm. **69**, 155 (1992). Also in *Proc. Workshop Physics at HERA*, 1991, DESY, Hamburg.

[14] G. Ingelman, A. Edin and J. Rathsman, Comp. Phys. Comm. **101**, 108 (1997).

[15] L. Lönnblad, Comp. Phys. Comm. **71**, 15 (1992).

[16] T. Sjöstrand, Comp. Phys. Comm. **82**, 74 (1994).

[17] H.L. Lai et al., Phys. Rev. **D 55**, 1280 (1997).

[18] D. Haidt, private communication (2002).

[19] K. Golec-Biernat and M. Wüsthoff, Phys. Rev. **D 59**, 014017 (1999);
K. Golec-Biernat and M. Wüsthoff, Phys. Rev. **D 60**, 114023 (1999).

[20] H. Jung, Comp. Phys. Comm. **86**, 147 (1995).

[21] ZEUS Coll., J. Breitweg et al., Eur. Phys. J. **C 12**, 393 (2000).

[22] ZEUS Coll., J. Breitweg et al., Eur. Phys. J. **C 6**, 603 (1999).

[23] H. Lim, *Measurement of the diffractive cross section.* Ph.D. Thesis, The Graduate School, Kyungpook National University, Taegu (Republic of Korea), 2002.

[24] H1 Coll., C. Adloff et al., Eur. Phys. J. **C 21**, 33 (2001).

[25] ZEUS Coll., S. Chekanov et al., Phys. Rev. **D**, 12007 (2003).

[26] L.N. Hand, Phys. Rev. **129**, 1834 (1963);
S.D. Drell and J.D. Walecka, Ann. Phys. (NY) **28**, 14 (1964);
F.J. Gilman, Phys. Rev. **167**, 1365 (1968).

[27] J.R. Cudell, K. Kang and S.K. Kim, Phys. Lett. **B 395**, 311 (1997).

[28] J. Bartels, J. Ellis, H. Kowalski, M. Wüesthoff, Eur. Phys. J. **C7**, 443 (1999).

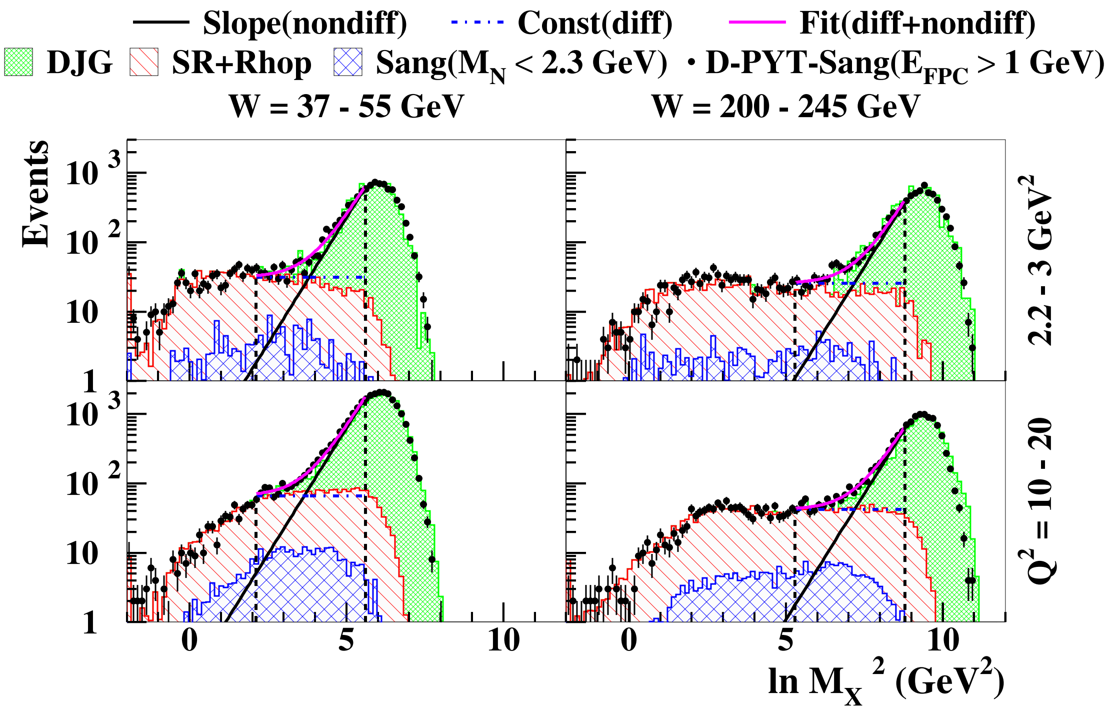

Figure 1: *Reaction $\gamma^* p \to X + anything$, where X is the system observed in the detector. Shown are distributions of $\ln M_X^2$, M_X in units of GeV, at the detector level for different Q^2, W bins. The full points with error bars show the data. The shaded areas show the non-diffractive contributions as predicted by DJANGOH. The diffractive contributions from $\gamma^* p \to X + p$ ($\gamma^* p \to X + N^{\rm dissoc}$, $M_N < 2.3$ GeV) as predicted by SATRAP+RHOP (SANG) are shown as dashed (cross-hatched) areas. The straight lines show the results for the non-diffractive contribution from fitting the sum of the diffractive and non-diffractive contributions in the $\ln M_X^2$ range delimited by the two vertical dashed lines.*

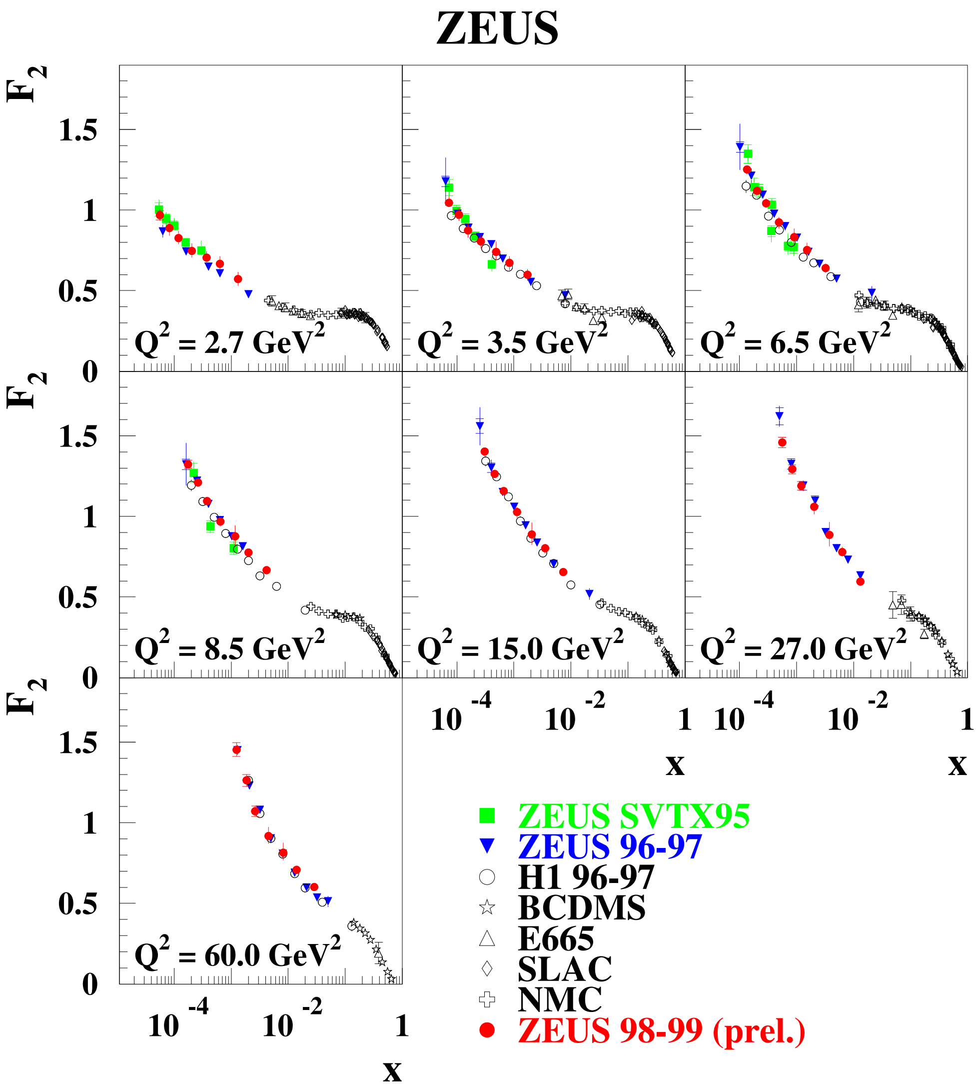

Figure 2: *The values of the proton structure function F_2 determined in this analysis are compared with those from other measurements for the Q^2-values indicated. The inner error bars show the statistical uncertainties and the full bars the statistical and systematic uncertainties added in quadrature.*

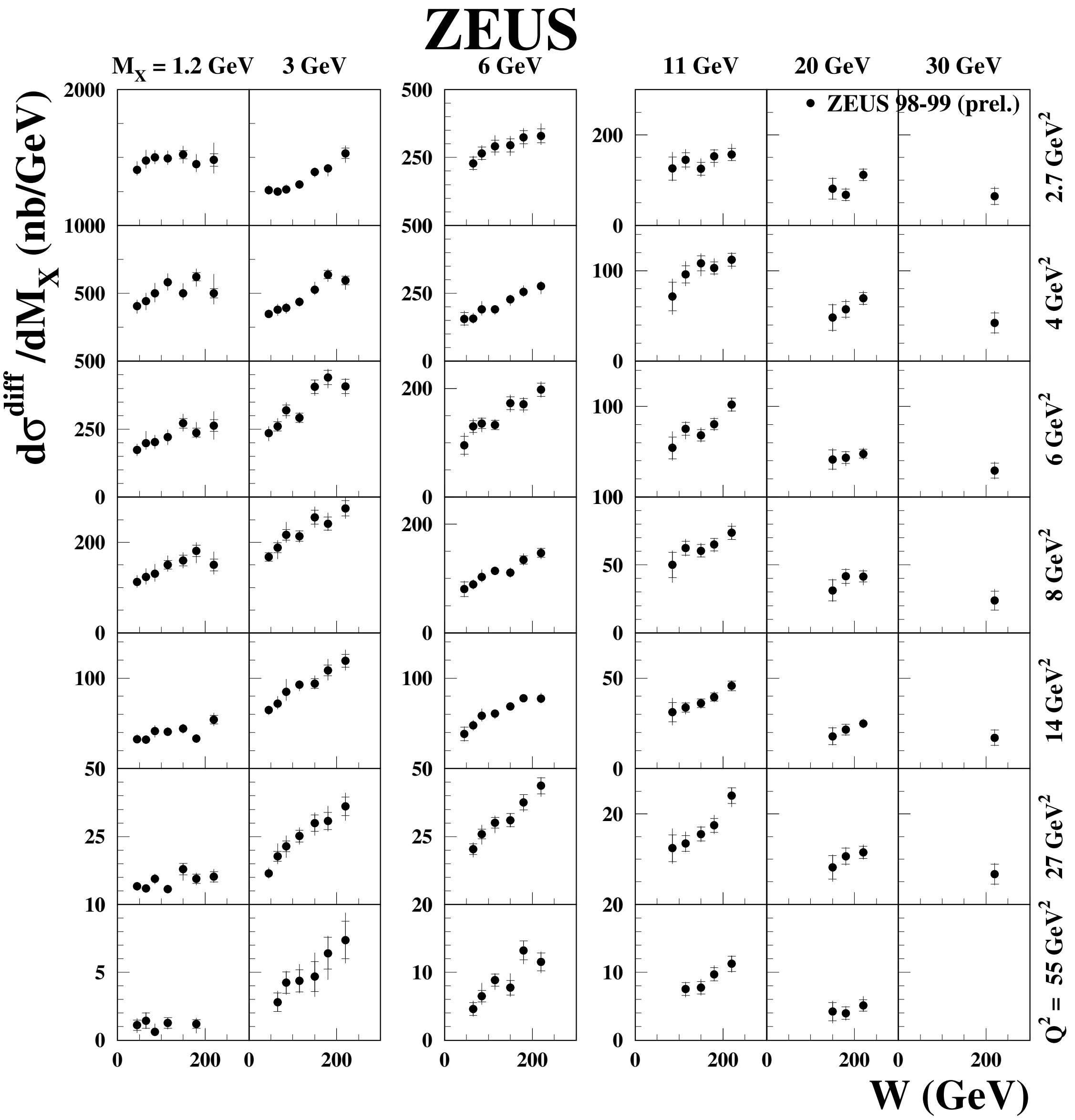

Figure 3: *The differential cross sections $d\sigma^{\mathrm{diff}}_{\gamma^* p\to XN}/dM_X$, $M_N < 2.3$ GeV, as a function of W for bins of M_X and Q^2. The inner error bars show the statistical uncertainties and the full bars the statistical and systematic uncertainties added in quadrature.*

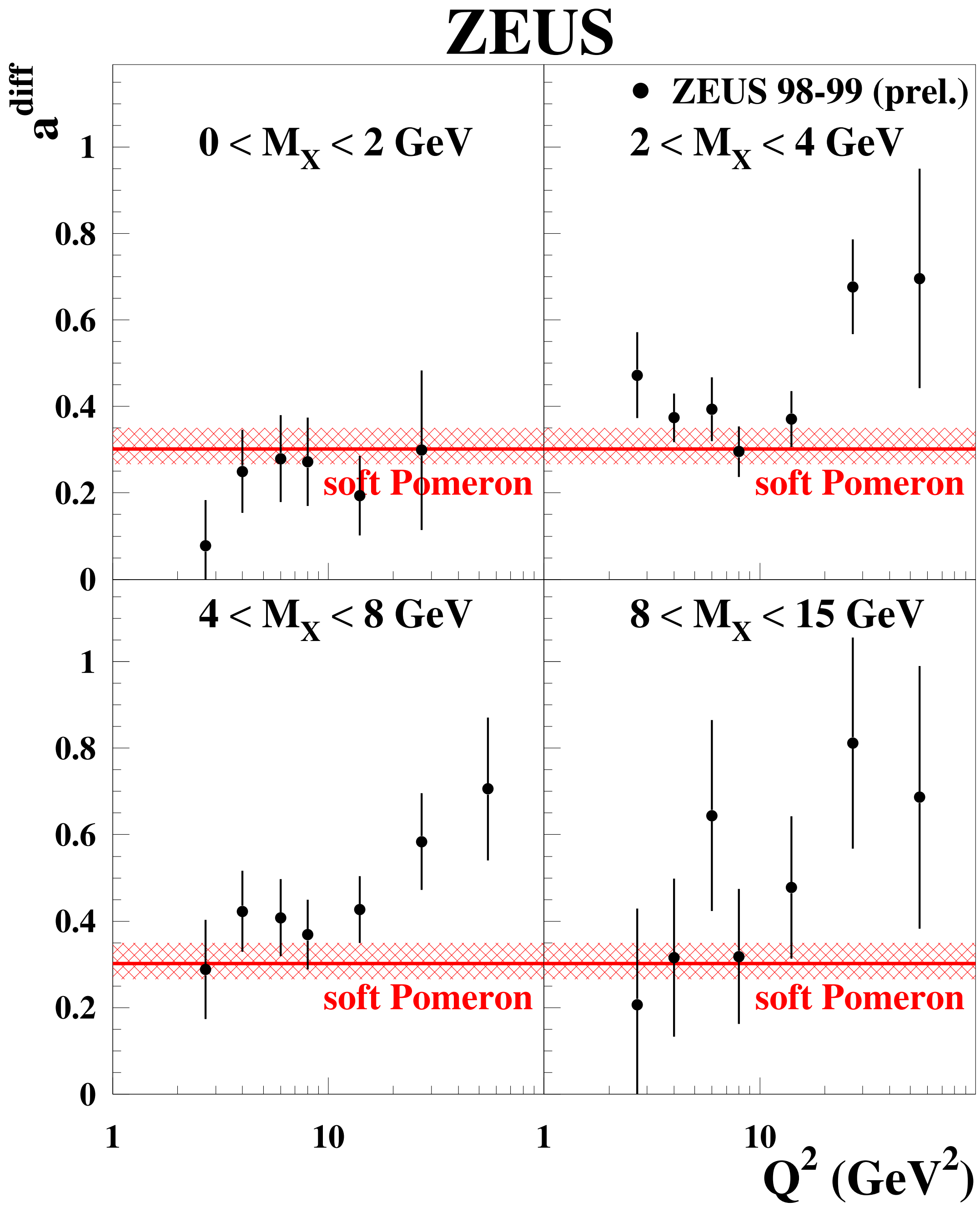

Figure 4: *The power $a^{\rm diff}$ obtained from fitting the diffractive cross section, $d\sigma^{\rm diff}_{\gamma^* p \to XN}(M_X, W, Q^2)/dM_X = h \cdot W^{a^{\rm diff}}$, as a function of Q^2 for the M_X-bins 0 - 2, 2 - 4, 4 - 8 and 8 - 15* GeV*. The shaded band shows the expectation for $a^{\rm diff}$ for a soft Pomeron.*

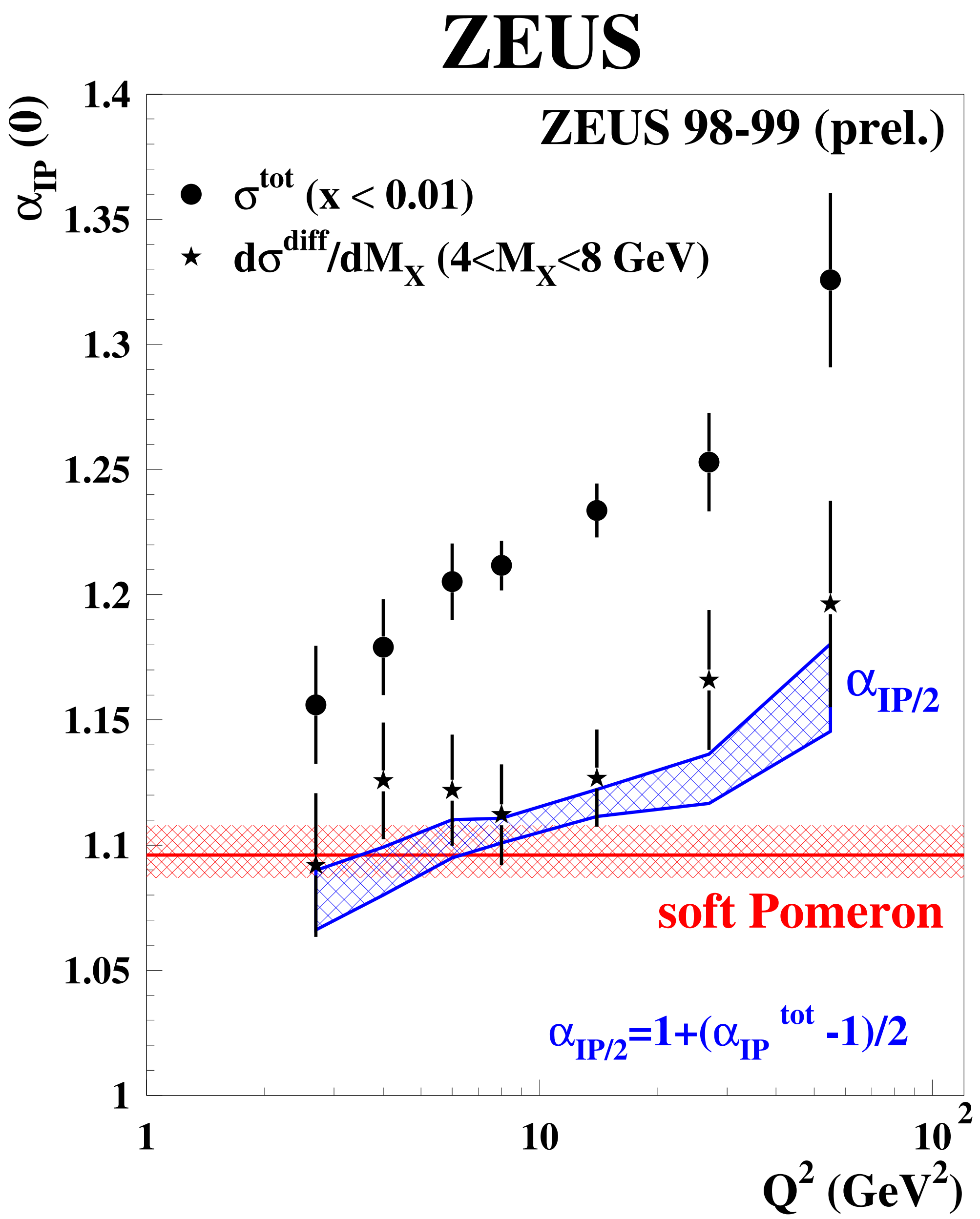

Figure 5: *The intercept of the Pomeron trajectory, $\alpha_{I\!P}(0)$, as a function of Q^2, obtained from the W-dependences of the total γ^*p cross section and from the diffractive cross section, $d\sigma^{\rm diff}_{\gamma^*p\to XN}(M_X, W, Q^2)/dM_X$ for $4 < M_X < 8$ GeV. The $\alpha_{I\!P}(0)$-values for the latter have been corrected for the t-dependence of $\alpha_{I\!P}$. The shaded band shows the expectation for a soft Pomeron. The cross hatched band represents 'half' of the W-rise of the total cross section, $\alpha_{I\!P/2} = 1+(\alpha^{\rm tot}_{I\!P}(0)-1)/2$.*

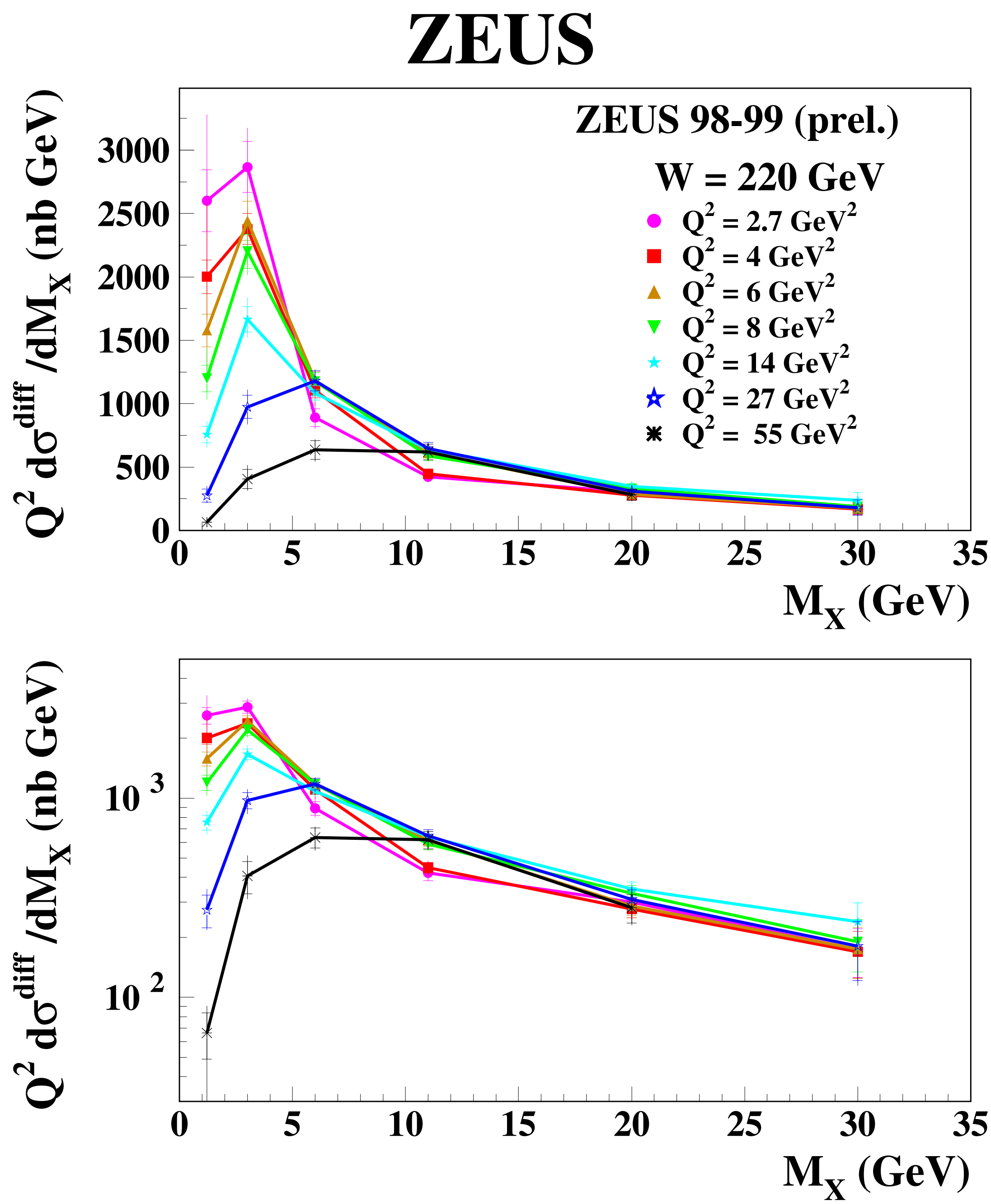

Figure 6: *The diffractive cross section multiplied by Q^2, $Q^2 \cdot d\sigma^{\rm diff}_{\gamma^* p \to XN}/dM_X$, $M_N < 2.3$ GeV, for $W = 220$ GeV, as a function of M_X for the Q^2 intervals indicated. Top: on a linear scale; Bottom: on a logarithmic scale. The inner error bars show the statistical uncertainties and the full bars the statistical and systematic uncertainties added in quadrature. The lines connect the points measured for the same value of Q^2.*

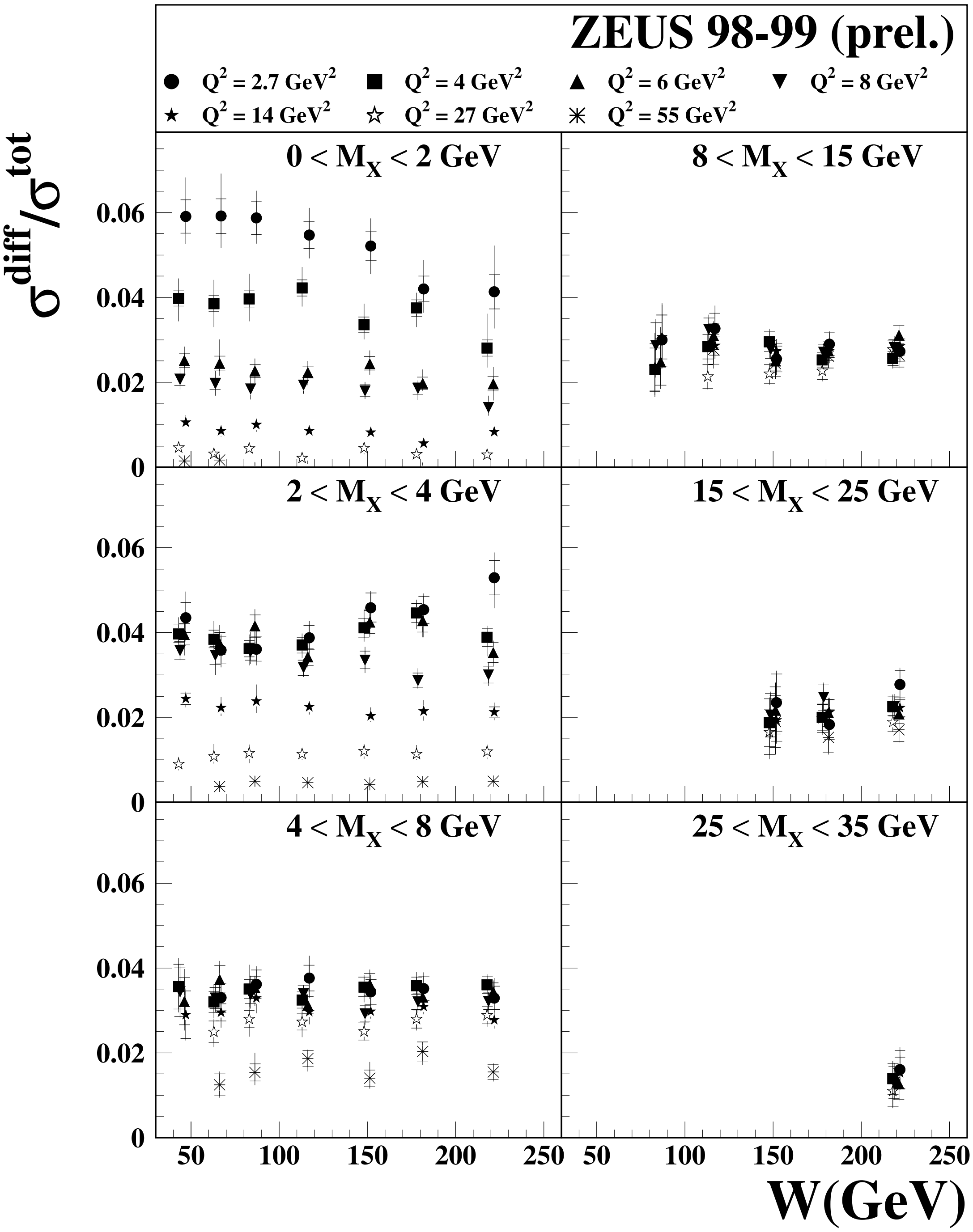

Figure 7: *The ratio of the diffractive cross section, integrated over the M_X intervals indicated, $\int_{M_a}^{M_b} dM_X d\sigma^{\rm diff}_{\gamma^* p\to XN, M_N<2.3{\rm GeV}}/dM_X$, to the total $\gamma^* p$ cross section, $r^{\rm diff}_{\rm tot} = \sigma^{\rm diff}/\sigma^{\rm tot}_{\gamma^* p}$, as a function of W for the M_X and Q^2 intervals indicated. The inner error bars show the statistical uncertainties and the full bars the statistical and systematic uncertainties added in quadrature.*

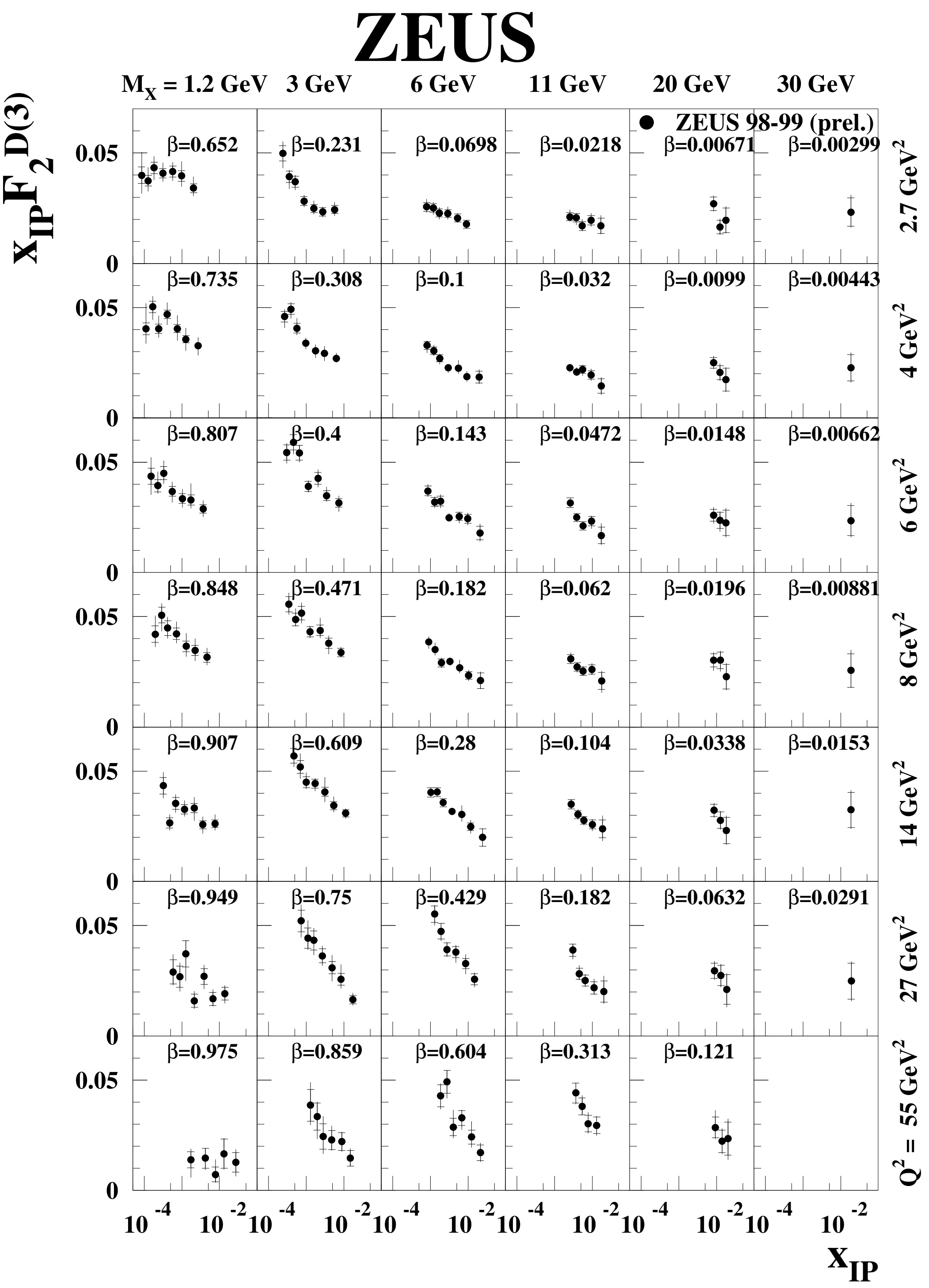

Figure 8: *The diffractive structure function of the proton multiplied by* $x_{\mathbb{P}}$, $x_{\mathbb{P}}F_2^{D(3)}$, *as a function of* $x_{\mathbb{P}}$ *for different regions of* Q^2 *and* β. *Also shown is the value of* β *for each bin. The inner error bars show the statistical uncertainties and the full bars the statistical and systematic uncertainties added in quadrature.*

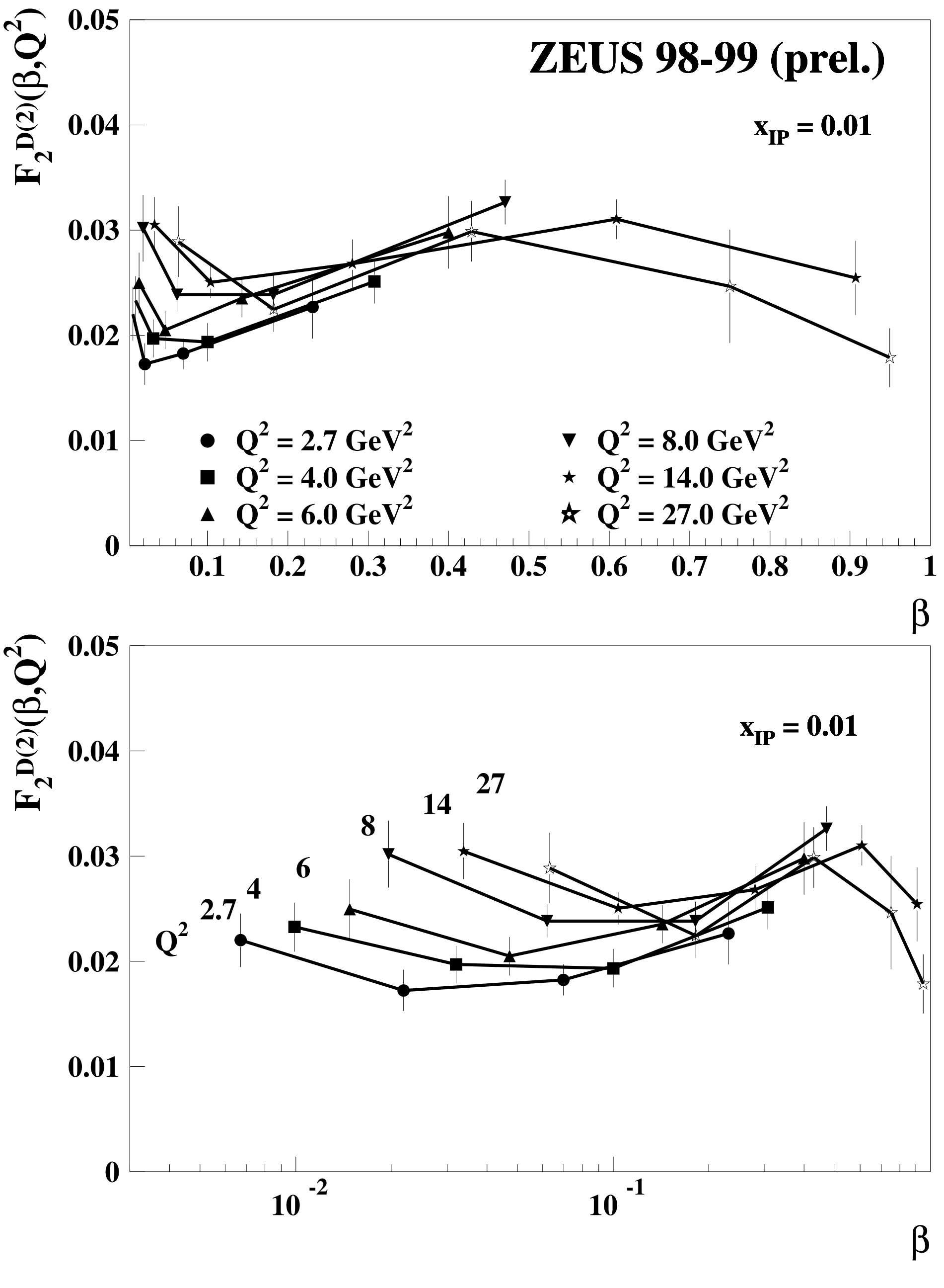

Figure 9: *The structure function $F_2^{D(2)}(\beta, Q^2)$ for $\gamma^* p \to XN, M_N < 2.3$ GeV, as a function of β, for the Q^2 values indicated, as extracted from the $x_{I\!P} F_2^{D(3)}$ values measured near $x_{I\!P} = 0.01$. The inner error bars show the statistical uncertainties and the full bars the statistical and systematic uncertainties added in quadrature. The straight lines connect measurements at the same value of Q^2.*

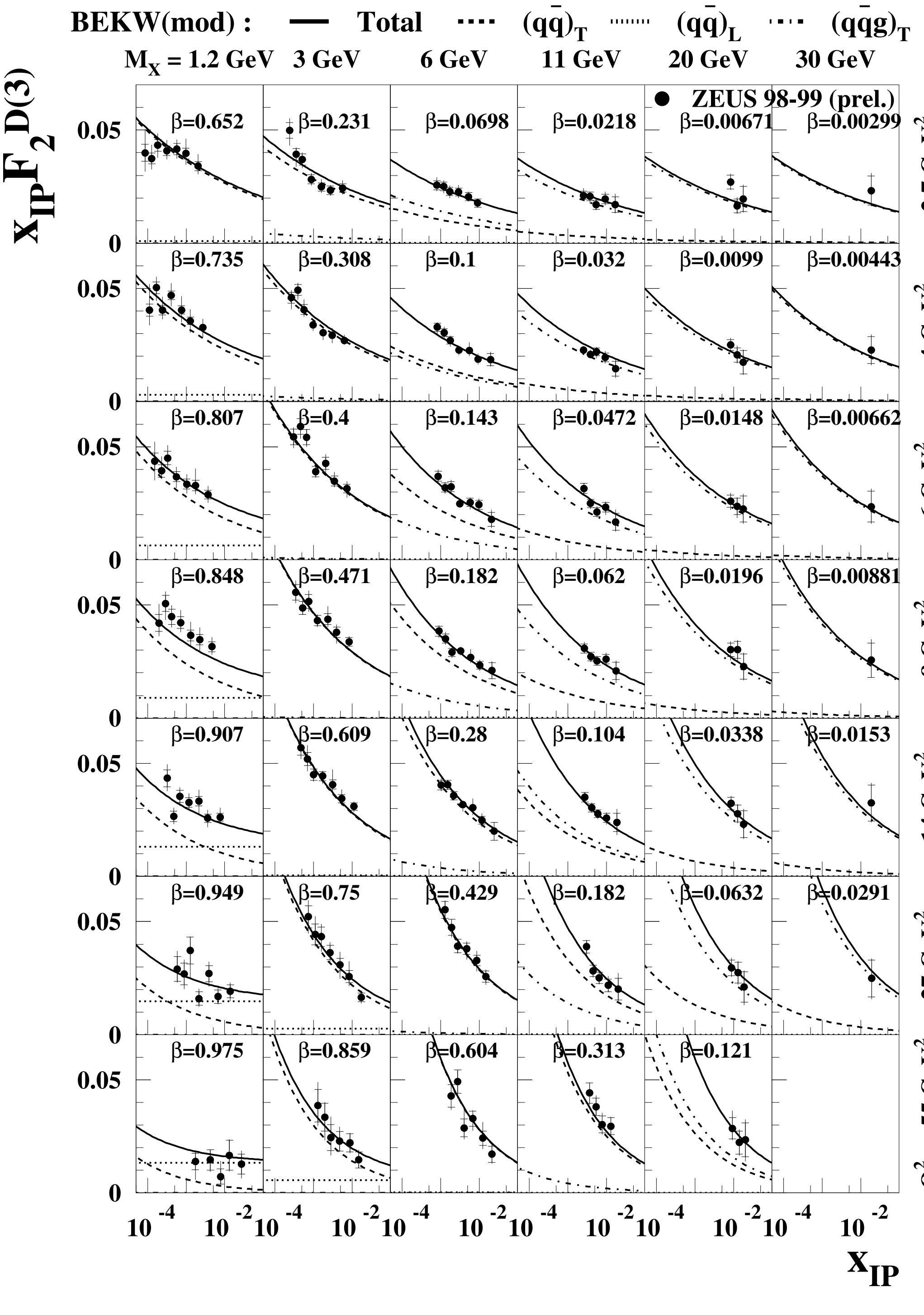

Figure 10: *The diffractive structure function of the proton multiplied by $x_{\mathbb{P}}$, $x_{\mathbb{P}}F_2^{D(3)}$, as a function of $x_{\mathbb{P}}$ for different regions of Q^2 and β. The curves show the result of the BEKW fit for the contributions from $(q\bar{q})$ for transverse (dashed) and longitudinal photons (dotted)and for the$(q\bar{q}g)$ contribution for transverse photons (dashed-dotted) together with the sum of all contributions (solid).*

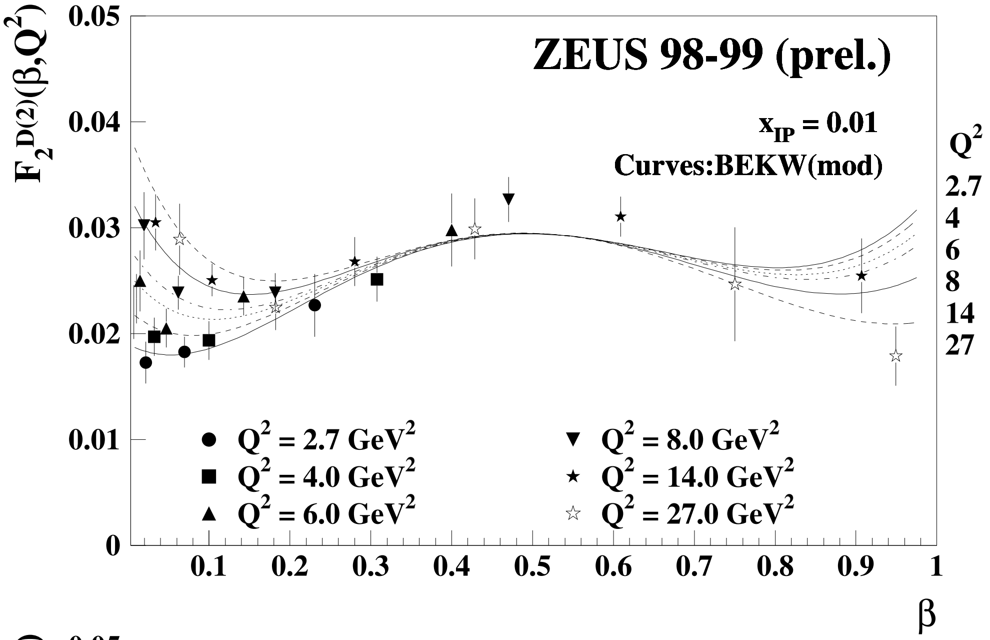

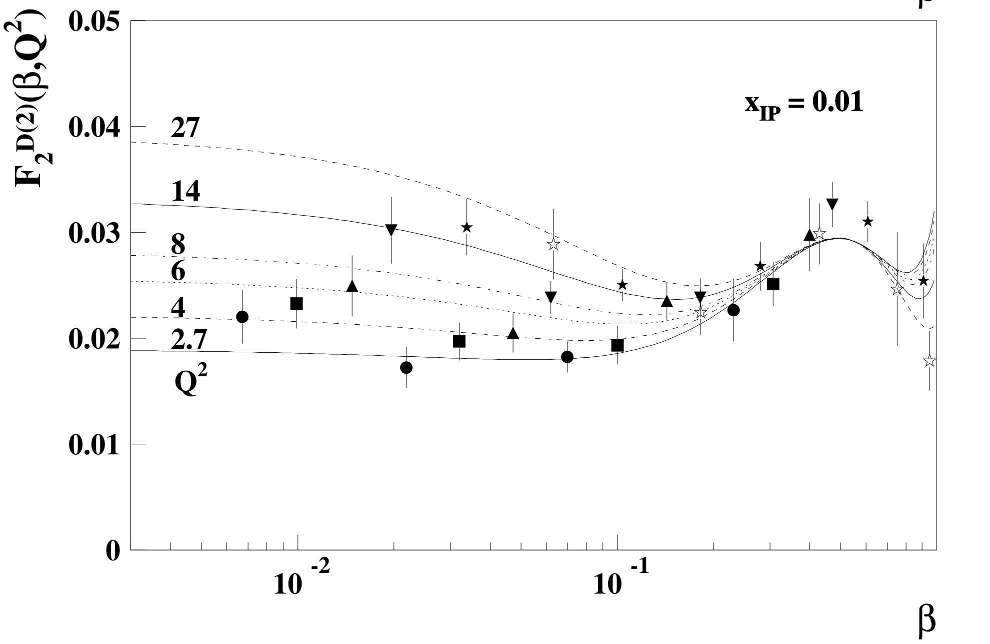

Figure 11: *The structure function $F_2^{D(2)}(\beta, Q^2)$ for $\gamma^* p \to XN, M_N < 2.3$ GeV, as a function of β for the Q^2 values indicated, as extracted from the $x_{I\!P} F_2^{D(3)}$ values measured near $x_{I\!P} = 0.01$. The inner error bars show the statistical uncertainties and the full bars the statistical and systematic uncertainties added in quadrature. The smooth curves show the results of the BEKW(mod) fit.*

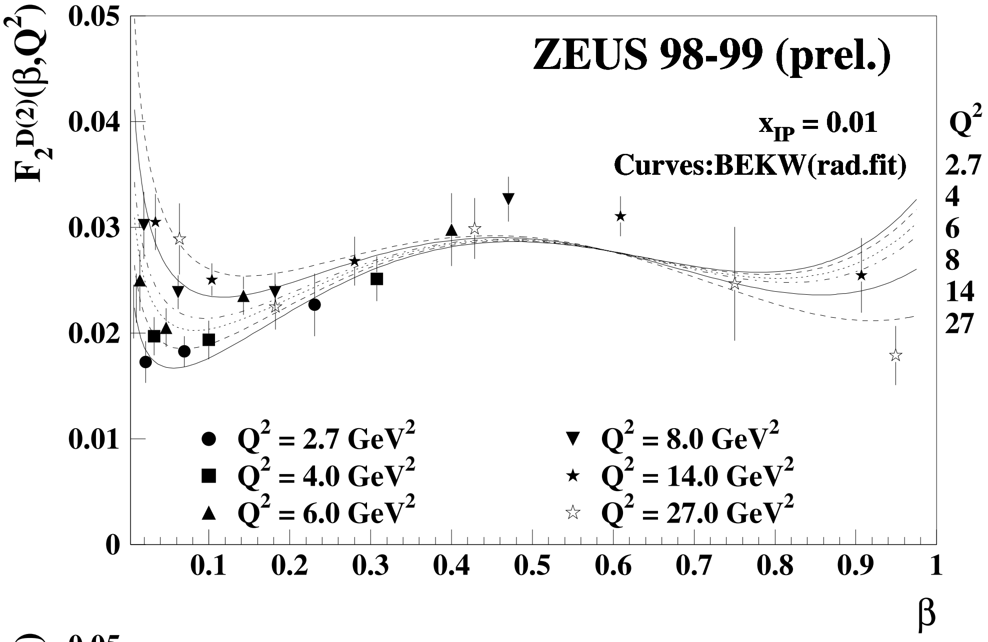

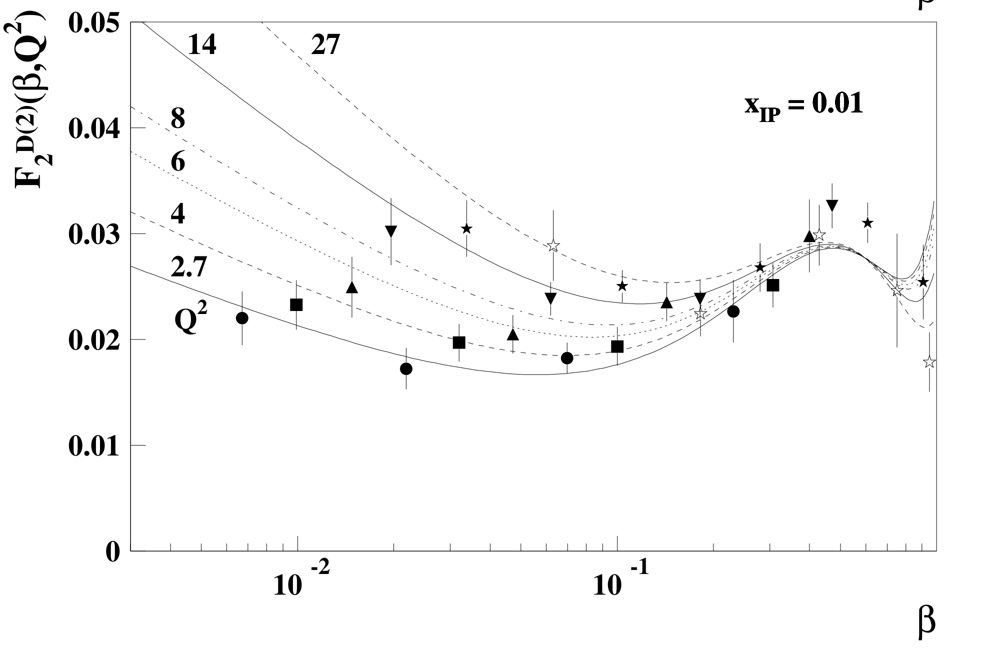

Figure 12: *The structure function $F_2^{D(2)}(\beta, Q^2)$ for $\gamma^* p \to XN, M_N < 2.3$ GeV, as a function of β for the Q^2 values indicated, as extracted from the $x_{I\!P} F_2^{D(3)}$ values measured near $x_{I\!P} = 0.01$. The smooth curves show the results of the radiation fit.*